

Defect-State Lasing in Photonic Lattices of Metal–Organic Microcavities

Mona Kliem, Thomas Kiel, Malin Kück, Stefan Meister, Andreas Mischok,*
Hartmut Fröb, Kurt Busch,* and Karl Leo*

Photonic band structure engineering has developed into an important technique for controlling the emission and interaction of photons and polaritons in microcavities (MCs). Herein, lasing from defect states (DSs) in photonic Kronig–Penney structures embedded into metal–organic MCs is demonstrated. As compared to the more delocalized lasing states associated with photonic bands, these DSs exhibit improved lasing thresholds that lie even below the lasing threshold of the metal-free cavity. The characteristics of these DSs are determined via full electrodynamic computations based on the discontinuous Galerkin time-domain method.

1. Introduction

The investigation of crystal lattices leads to the observation of a dispersion band structure both in solid-state physics and in photonics. Besides “allowed” bands, these band structures exhibit for electrons and photons, respectively, “forbidden” energy ranges (bandgaps [BGs]), and “forbidden” wavelength ranges (stop bands).^[1] Introducing defects into perfect crystals leads to the formation of trap states in the “forbidden” ranges, often unwanted

in e.g., purified intrinsic semiconductor materials but extremely versatile when being controlled directly. For instance, looking at inorganic and organic semiconductor devices, there exists an immense benefit related to p- and n-dopants as defects with energies within the BGs.^[2–4] Similarly, in photonics, defects can create very useful high-quality cavities.^[5] The most prevalent class of such defects is that of the distributed Bragg reflector (DBR) microcavities (MCs), where a 1D photonic crystal of alternating $\lambda/4$ layers of high and low refractive index is “disturbed” by an active $\lambda/2$ cavity layer.^[6] In turn, the resulting cavity characteristics can be altered by adding in-plane (lateral) patterning, e.g., to facilitate 3D confinement of light.

Such optical confinement has been under investigation for a long time. Resulting from the micron-scale trapping of light, discrete modes in angular-resolved spectra of MCs with individual 0D boxes^[7] and individual 1D wires^[8] have been analyzed and utilized for low-threshold lasing.^[9,10] In addition, photonic bands and BGs of chains of boxes^[11,12] or arrays of wires^[13–15] have been facilitated and observed, thus creating another photonic crystal in the lateral defect plane. Such structures are often fabricated by etching micropillars into MCs via electron beam lithography and reactive-ion etching^[12,16] or direct laser writing.^[10] In our case, in-plane (lateral) photonic confinement is realized by adding a thin silver layer that is deposited in between the bottom DBR and the active layer. Subsequently, structuring this silver layer via photolithography into parallel stripes facilitates the interaction of cavity photons and Tamm plasmon polaritons (TPPs).^[17–21] As a result, the original cavity mode of a DBR MC is spectrally red-shifted. In other words: By creating a 1D grating of silver, an in-plane photonic crystal is formed that exhibits a band structure with allowed and stop bands^[22] similar to the vertical DBR cavity. In turn, a controlled defect can be introduced into the in-plane pattern and this introduces trap states within its dispersion band structure, thus facilitating highly confined optical modes. Similar observations have recently been made in topological edge states of 1D polaritonic micropillar lattices^[23] which create highly confined, discrete states within the polariton band structure.

Here, we utilize the formation of a photon band structure within metal–organic MCs by controlled patterning of in-plane silver grating.^[24] Introducing defects into the photonic crystal, we observe the resulting trap states via angle-resolved microphotoluminescence spectroscopy. Finally, the plasmonically induced

M. Kliem, Dr. S. Meister, Dr. A. Mischok, Dr. H. Fröb, Prof. K. Leo
Dresden Integrated Center for Applied Physics and Photonic Materials
Technische Universität Dresden
01062 Dresden, Germany
E-mail: am470@st-andrews.ac.uk; karl.leo@tu-dresden.de

T. Kiel, M. Kück, Prof. K. Busch
Theoretical Optics and Photonics
Institut für Physik
Humboldt-Universität Berlin
Newtonstraße 15, 12489 Berlin, Germany
E-mail: kbusch@physik.hu-berlin.de

Dr. A. Mischok
Organic Semiconductor Centre
SUPA, School of Physics and Astronomy
University of St. Andrews
North Haugh, St. Andrews KY16 9SS, UK

Prof. K. Busch
Max-Born-Institut
Max-Born-Straße 2A, 12489 Berlin, Germany

 The ORCID identification number(s) for the author(s) of this article can be found under <https://doi.org/10.1002/adpr.202000116>.

© 2020 The Authors. Advanced Photonics Research published by Wiley-VCH GmbH. This is an open access article under the terms of the Creative Commons Attribution License, which permits use, distribution and reproduction in any medium, provided the original work is properly cited.

DOI: 10.1002/adpr.202000116

optical confinement is exploited to enhance the performance of the lasing system, especially to decrease the threshold of our hybrid inorganic–organic microlasers.

2. Experimental Section

The investigated MC consisted two identical DBRs made of 21/2 pairs of silicon dioxide (SiO₂) and titanium dioxide (TiO₂) layers with quarter-wavelength thicknesses, i.e., $d_{\text{SiO}_2} \approx 110$ nm and $d_{\text{TiO}_2} \approx 72$ nm, respectively. Between the DBRs, a thin patterned silver layer ($d_{\text{Ag}} \approx 33$ nm) and the active layer with an optical thickness of $\lambda/2$ (see Figure 1a) were evaporated subsequently. As active layer, we used an organic host: guest system, consisting of tris(8-hydroxyquinolin)aluminum (Alq₃) as matrix material and 4-(dicyanomethylene)-2-methyl-6-[p-(dimethylamino)-styryl]-4-pyran (DCM at 2 wt%) as emitter.

The structuring of the silver layer was done by a photolithographic lift-off process. The quality of the resulting silver edges was demonstrated by atomic force microscopy, as shown in Figure S1, Supporting Information. The resulting structures were stripe-like patterns with period lengths p between 5.0 and 7.0 μm . Here, the widths of the silver and organic stripes are denoted by a and b , respectively. Introducing a defect into the pattern leads to a distance between two adjacent silver stripes of d (see Figure 1b).

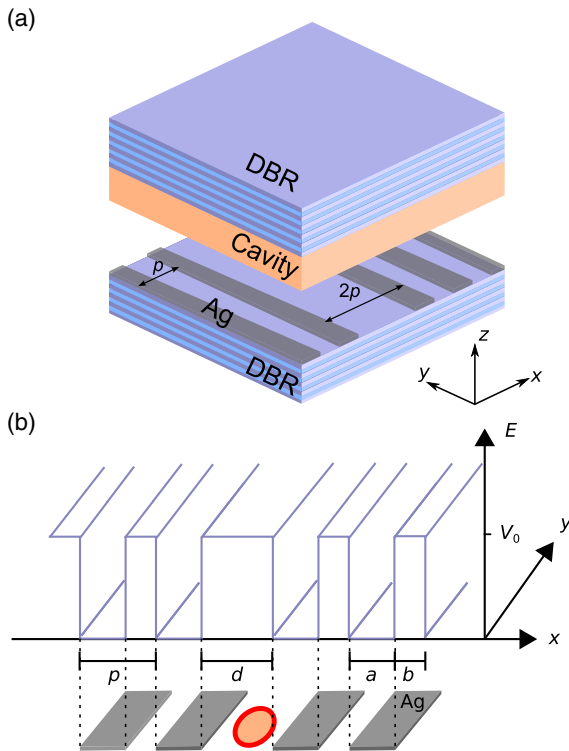


Figure 1. a) Schematic of the MC. b) Potential landscape of the periodic stripe-like pattern with defects. The parameters of the potential landscape are period p , width of the defect d , width of the silver stripes/potential well a , width of the organic stripes/potential barrier b , and potential height V_0 . The laser spot position during the defect measurement is marked in red.

For optical excitation below and above threshold, we use either a continuous wave (CW) laser diode (405 nm) or a pulsed solid-state laser (532 nm, 1.5 ns pulse length at 2 kHz). The excitation beam was focused on the sample using a $\times 25$ microscope objective, resulting in a spot with a diameter of ≈ 7 μm . Far-field emission was collected by a $\times 63$ objective (NA = 0.8) and projected on the entrance slit of a 0.6 m imaging spectrometer, recorded by a cooled charge-coupled device. The results of this measurement were angle-resolved emission spectra of high quality taken at ambient conditions.

3. Theoretical Model

For a better understanding of the design of the structures, the lasing dynamics of the organic MCs with varying internal silver metal gratings are computed with a discontinuous Galerkin time-domain (DGTd) method.^[25] The DGTd method is used to solve the macroscopic Maxwell's equations. Here, SiO₂ is modeled with a constant relative permittivity $\epsilon = 2.165$. The TiO₂ layers of the DBRs as well as the silver grating are fully modeled by appropriate Drude–Lorentz models describing their susceptibilities (see [26,27] for fit parameters). In addition, a nonlinear four-level system material model^[28,29] is used to describe the Alq₃:DCM organic material.

Two optically active transitions are assumed (see Figure 2), for which the transition polarizations couple into Maxwell's curl equations

$$\nabla \times \vec{E} = -\partial_t \vec{B} \quad (1)$$

$$\nabla \times \vec{H} = \epsilon_{\text{bg}} \partial_t \vec{E} + N_{\text{dye}} (\partial_t \vec{P}_{03} + \partial_t \vec{P}_{12}) \quad (2)$$

The dipole transitions are described by driven harmonic oscillators for the transition polarizations

$$\partial_t^2 \vec{P}_{03} + \gamma_{03} \partial_t \vec{P}_{03} + \omega_{03}^2 \vec{P}_{03} = -\Delta N_{03} \zeta_{03} \vec{E} \quad (3)$$

$$\partial_t^2 \vec{P}_{12} + \gamma_{12} \partial_t \vec{P}_{12} + \omega_{12}^2 \vec{P}_{12} = -\Delta N_{12} \zeta_{12} \vec{E} \quad (4)$$

where $\Delta N_{ij} = N_j - N_i$ denotes the population inversion between the i -th and j -th level. Accordingly, the level occupation densities are modeled with laser rate equations

$$\partial_t N_3 = -\frac{N_3(1 - N_2)}{\tau_{23}} - \frac{N_3(1 - N_0)}{\tau_{03}} + \frac{\vec{E} \cdot \partial_t \vec{P}_{03}}{\hbar \omega_{03}} \quad (5)$$

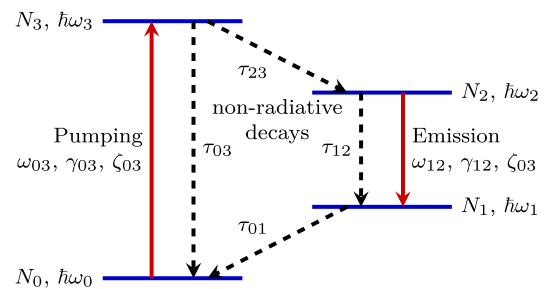


Figure 2. Four-level scheme of the material model for the Alq₃:DCM active material used in the DGTd method.

$$\partial_t N_2 = \frac{N_3(1 - N_2)}{\tau_{23}} - \frac{N_2(1 - N_1)}{\tau_{12}} + \frac{\vec{E} \cdot \partial_t \vec{P}_{12}}{\hbar\omega_{12}} \quad (6)$$

$$\partial_t N_1 = \frac{N_2(1 - N_1)}{\tau_{12}} - \frac{N_1(1 - N_0)}{\tau_{01}} - \frac{\vec{E} \cdot \partial_t \vec{P}_{12}}{\hbar\omega_{12}} \quad (7)$$

$$\partial_t N_0 = \frac{N_3(1 - N_0)}{\tau_{03}} + \frac{N_1(1 - N_0)}{\tau_{01}} - \frac{\vec{E} \cdot \partial_t \vec{P}_{03}}{\hbar\omega_{03}} \quad (8)$$

To model the actual Alq₃:DCM 190 nm-thick material layer, we use an emitter density of $N_{\text{dye}} = 0.25 \text{ nm}^{-3}$. The transition frequencies $\omega_{03} = 4.01e + 15 \text{ rads}^{-1}$ and $\omega_{12} = 2.94e + 15 \text{ rads}^{-1}$ as well as the dephasing rates $\gamma_{03} = \gamma_{12} = 4.8e + 14 \text{ rads}^{-1}$ can be estimated from Lorentzian fits of the absorption and photoluminescence spectra. The coupling strength $\zeta_{12} = \frac{6\pi\epsilon_0\epsilon_{\text{bg}}c^3}{\omega_{12}^2\tau_{12}} = 5.68 \times 10^{-8} \text{ Am}^2\text{V}^{-1}\text{s}^{-1}$ can be determined from the background permittivity $\epsilon_{\text{bg}} = 2.8$ and the spontaneous emission time $\tau_{12} = 4 \text{ ns}$ ^[28]. The coupling strength $\zeta_{03} = 3.63e - 07 \text{ Am}^2\text{V}^{-1}\text{s}^{-1}$ is estimated from the absorption spectrum with a fitted Lorentz pole strength. The nonradiative decay times $\tau_{01} = 50 \text{ fs}$ and $\tau_{23} = 100 \text{ fs}$ are chosen much larger than the field oscillation period and orders of magnitude smaller than the spontaneous emission times. The nonradiative decay times of the dipole transitions are assumed to be much larger $\tau_{03}, \tau_{12} \gg \tau_{01}, \tau_{23}$ and are consequently neglected ($\tau_{03}, \tau_{12} \rightarrow \infty$).

This four-level system is optically pumped, using a Gaussian focused beam excitation^[30] of the MC. The time-modulated pulse lasts 4 ps, i.e., significantly longer than the nonradiative decay times of the four-level system. We then distinguish four excitation positions for the focus of the effectively 2D system: Excitation of a metal-free organic MC, of a MC with silver grating in a gap, or on a silver stripe and of the defect system (see red spot in Figure 1). The computations are carried out for MCs with a grating period of $p = 5 \mu\text{m}$ and silver stripe width of $a = 3.1 \mu\text{m}$. The defect width is $d = 4 \mu\text{m}$. The computational domain contains four periods in lateral direction (periodic superlattice) to sufficiently accommodate the $6 \mu\text{m}$ -wide pump beam. We use a 532 nm carrier wave which is ramped up and down within a 4 ps pulse, guaranteeing a sufficiently slow excitation of the nonlinear organic material. It is computed on the total-field/scattered-field (Tf/Sf) contour^[25,29] used to launch the focused beam into the computational domain. The field-strength variation of the pump pulse sets the input energy. Correspondingly, the emitted energy

$$E_{\text{out}} = -\frac{2}{\pi} \int_{-\delta\omega}^{\delta\omega} d\omega \int_{A_c} d\vec{f} \cdot \langle \vec{S} \rangle_T(\vec{r}, \omega_{\text{em}} + \omega) \quad (9)$$

in the lasing frequency window $\omega_{\text{em}} \pm \delta\omega$ is computed by recording the time-averaged Poynting vector $\langle \vec{S} \rangle_T$ on contours with area A_c both below (transmission contour) and above (Tf/Sf contour) the cavity (see green and red lines in Figure 6).

The DGTD simulations are conducted using a custom code^[25] on an high performance computing cluster with $40 \times$ Dual Intel Xeon E5-2670 with 16 cores at 2.6 GHz.

4. Results and Discussion

4.1. Below-Threshold Investigation

The in-plane photonic potential of a MC containing a stripe-like pattern is shown in Figure 1b. Here, the addition of silver stripes creates an array of rectangular potential barriers due to the formation of TPP states. The resulting structure shows high optical quality despite the addition of parasitic absorption of the silver layer.^[22] In comparison to an unpatterned thin silver film, the patterning then allows to fully make use of the confining properties with minimal loss in optical quality.

When the periodic, defect-free silver pattern is excited below lasing threshold, it exhibits a far-field emission spectrum that follows the photonic band structure of a periodic 1D Kronig-Penney potential.^[22] This is shown in Figure 3a,b for period lengths p of 6.0 and 5.0 μm , respectively. Here, the k_x component of the in-plane momentum is shown in units of $(a+b)/\pi$, which in turn equals the number of Brillouin zones. For both period lengths, discrete states below the potential barrier are detected. Above the potential barrier dispersive states are visible. Those states form “allowed” bands as well as “forbidden” energy BGs. For a period of $p = 5.0 \mu\text{m}$ a π -like lowest Bloch state and for $p = 6.0 \mu\text{m}$ a 2π -like lowest Bloch state is observed. For comparison, the far-field emission spectra of the bare organic cavity are shown in Figure S2, Supporting Information.

Introducing the defect into the grating disturbs this photonic band structure. Analogous to defect states (DSs) in crystal lattices, we observe additional nondispersive states, so-called DSs (see red circles in Figure 3c, d), which are spectrally located in the BG. For both period lengths, one central defect mode at $k_x = 0$ and one additional defect mode at higher energies are detected. For $p = 5.0 \mu\text{m}$ the central DS is spectrally located at $\lambda_{\text{DS1}} = 644 \text{ nm}$, whereas the corresponding BG ranges from $\lambda_{\text{BG1}} = 644$ to 647 nm. The second DS has a wavelength of $\lambda_{\text{DS2}} = 640 \text{ nm}$, with the corresponding BG ranging from $\lambda_{\text{BG2}} = 639.5$ to 641.5 nm. For $p = 6.0 \mu\text{m}$ we see similar results. The wavelength of the central defect mode equals $\lambda_{\text{DS1}} = 645 \text{ nm}$ with the corresponding BG ranging from $\lambda_{\text{BG1}} = 645$ to 647.5 nm. The second DS is spectrally located at $\lambda_{\text{DS2}} = 643 \text{ nm}$ and the corresponding BG ranges from $\lambda_{\text{BG2}} = 642$ to 644 nm. The nondispersive nature of these DS points toward a high degree of confinement, being essentially fully trapped at the defect position. In addition, the DS exhibits a large spread in k -space, further indicating a high degree of localization in real space.

4.2. Above-Threshold Investigation

Increasing the pump intensity above lasing threshold changes the far-field image. For the defect-free pattern (period lengths of $p = 6.0 \mu\text{m}$ and $p = 5.0 \mu\text{m}$), several equidistant laser modes at wavelengths of $\lambda = 643 \text{ nm}$ (2π state lasing) and $\lambda = 644 \text{ nm}$ (π state lasing) are measured (see Figure 4a,e). Lasing occurs at the edges of Brillouin zones, where photonic BGs lead to a high photonic density of states. Therefore, the spacing of the laser modes depends on the period length of the grating. Increasing the length of the period results in decreasing spacing (for a more detailed explanation see the study by Mischok

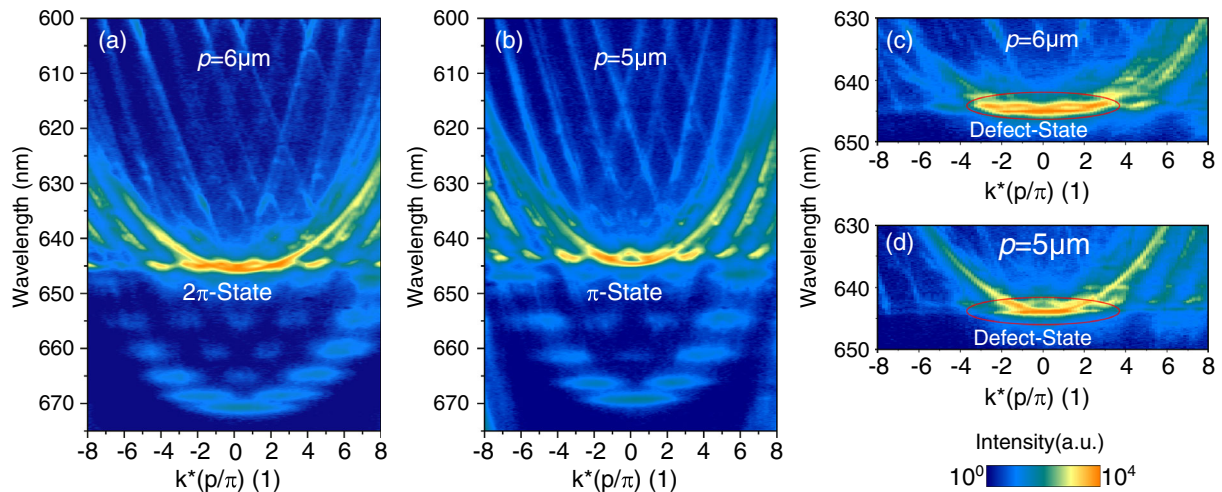


Figure 3. a,b) Below-threshold far-field image of stripe-like pattern with a) $p = 6.0 \mu\text{m}$ showing a 2π -like lowest Bloch state and b) $p = 5.0 \mu\text{m}$ showing a π -like lowest Bloch state. c,d) Below-threshold far-field image of the stripe-like pattern with defect and c) $p = 6.0 \mu\text{m}$ and d) $p = 5.0 \mu\text{m}$.

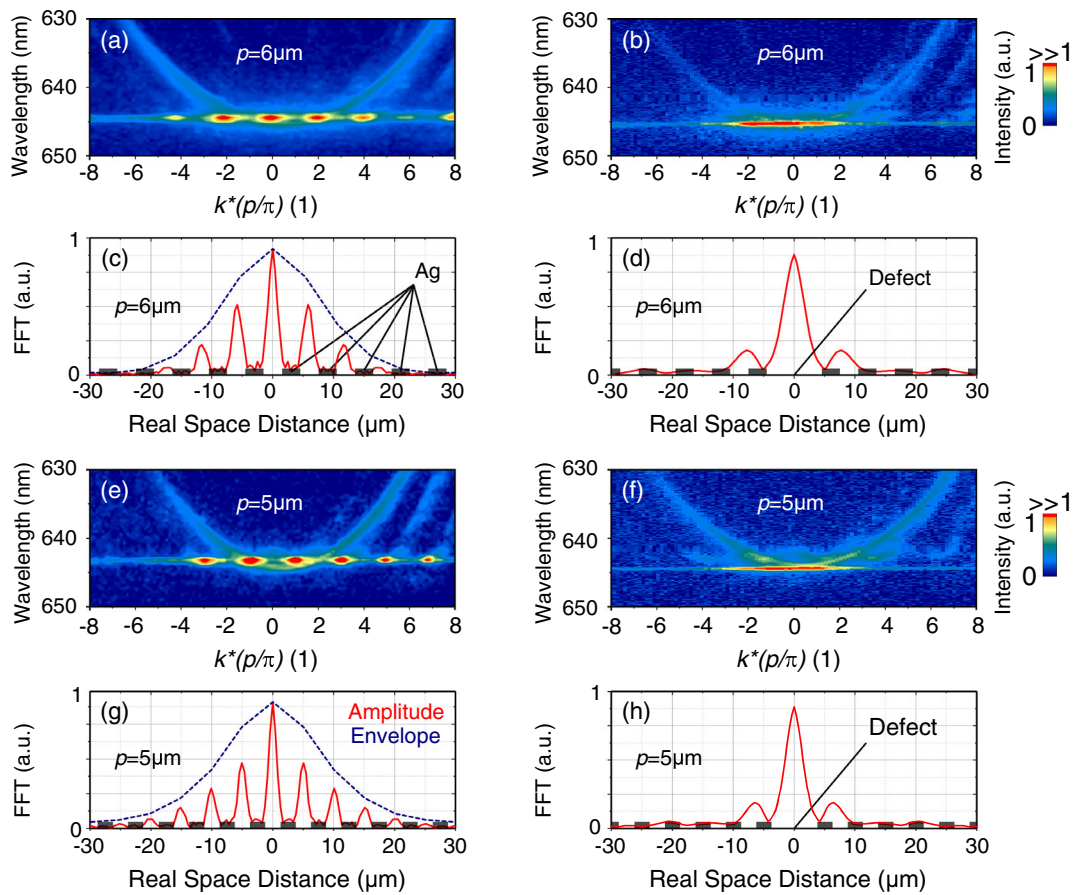


Figure 4. a,b) Above-threshold Fourier spectrum of grating with $p = 6.0 \mu\text{m}$ a) without and b) with a defect in the grating. c,d) FFT of (a) and (b), respectively, showing the real-space extension of the coherent laser mode. e,f) Above-threshold Fourier spectrum of grating with $p = 5.0 \mu\text{m}$ e) without and f) with a defect in the grating. g,h) FFT at the peak emission wavelength of (e) and (f), respectively, showing the real-space extension of the coherent laser mode.

et al.^[31]). The corresponding real-space extensions of the coherent laser modes are calculated with the help of Fast Fourier transform (FFT) and are shown in Figure 4c,g, respectively. We observe the formation of phase-locked extended supermodes, coupling emission over several grating periods.^[13,31]

Introducing a DS into the grating also changes the far-field image of the laser modes above the lasing threshold (see Figure 4b,f). Here, the confined DS (at $k_x = 0$) clearly exhibits the lowest lasing threshold in this system and starts to lase, showing a very broad expansion in k -space, thus indicating a very narrow and defined laser mode in real space. This is confirmed by the FFT images (Figure 4d,f), showing the lasing mode located within the defect in periodic patterning. We observe a much narrower lasing mode in real space, exhibiting an almost tenfold reduction in size and a strong confinement of the lasing mode within the defect. In addition, the linewidth of the lasing mode decreases substantially compared with defect-free supermodes.

As shown in Figure 5, the nonlinear transition into the regime of stimulated emission was measured for an organic MC without metal, with silver pattern, and with silver pattern inheriting a defect. The threshold of the purely organic MC corresponds to a pump intensity of 2.2 nJ. The threshold increases to 8.9 nJ due to the implementation of the silver stripe pattern. Here, the additional parasitic absorption introduced by the metal film increases losses in the cavity and thus slightly reduces the quality of the optical cavity, even if the supermode tries to avoid metallic areas. Introducing a defect into the pattern reduces the threshold significantly to 1.7 nJ. Therefore, the threshold is not only smaller in comparison with the defect-free pattern, but also as the metal-free MC. To verify the nonlinear behavior of the input–output curves, Maxwell–Bloch equations were used to fit the data.^[32,33]

4.3. DGTD Computations

To obtain a deeper understanding of the interplay of the MC lasing modes and their contributions to the lasing threshold,

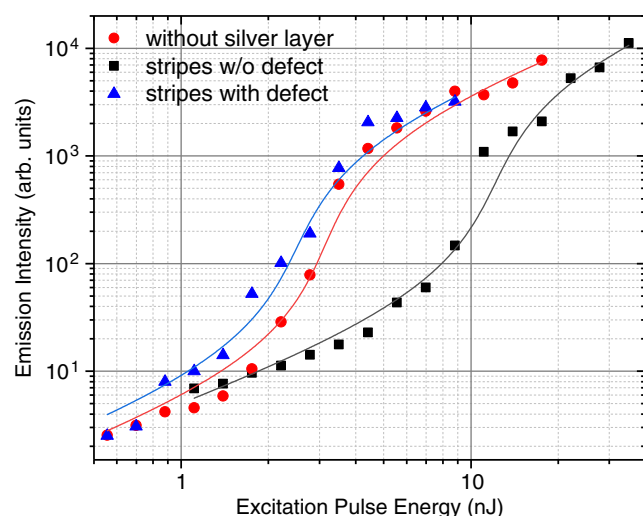


Figure 5. Input–output curves of a MC without metal (red dots), with silver stripe grating (black squares) and with a grating including a defect (blue triangles). The period length of the grating is $p = 7.0 \mu\text{m}$. Maxwell–Bloch equations were used to fit the data.

we additionally carry out DGTD computations. The computation of the lasing thresholds involves three steps, which are exemplarily presented for the defect excitation of the MC system using 17/2 pairs of SiO_2 and TiO_2 layers as DBRs.

The first step is the full time-dependent computation of the electromagnetic field accompanied by the laser rate equations and the associated coupling with transition polarizations.^[28,29] In Figure 6a we show the time-dependent electric field strength for a preset excitation pulse, just above the lasing threshold, in a vertical cut through the center of the 4 m defect of the MC. For times $t < 4$ ps, the excitation pulse is launched from the Tf/Sf contour (red line) into the computational domain. Parts of this pulse are reflected resulting in the interference pattern between the top boundary of the DBR and the Tf/Sf contour. Above this contour only the scattered, i.e., the reflected and emitted, field is computed. Below the DBR we observe a small amount of transmitted field. After the excitation pulse a single-emission pulse can be observed at around $t \approx 6$ ps. Here, only a single pulse is observed, as the system is operated far away from a CW regime and the population inversion ΔN_{12} between the two emission levels is just sufficiently raised to provide a single-emission burst. Figure 6b shows the population inversion ΔN_{12} at $t_{\text{em}} = 6$ ps, which roughly follows the Gaussian profile of the excitation beam. In Figure 6c we show the spatially resolved emission field pattern at time $t_{\text{em}} = 6$ ps. In accordance with the experimental observations, the field is strongest in the defect gap of the silver grating included in the DBR. In comparison, a defect-free grating as shown in Figure 6d shows a much weaker confinement and the field is extended in plane. In addition, we observe some waveguiding of the field along the DBR structure, as the DGTD computations are naturally conducted with periodic supercells. The period of this supercell is chosen just to be large enough, that the contribution of the guided field scattered from silver gratings is negligible for the overall emitted energy.

The second step is to compute the energy balance of the system. For this, we analyze the emitted and reflected power from the scattered field on both contours below and above the MC. Figure 7a shows the dependence of the scattered power P on the wavelength and energy of the input pulse for the defect setup. Here, the input pulse energy is determined by the peak field strength of the excitation beam for a given pulse shape. While we observe the reflected and transmitted power of the excitation beam for $\lambda \approx 532$ nm, we also can see two emerging laser modes around $\lambda \approx 640$ nm for sufficiently high input energies. Depending on the excitation beam and the geometry of grating, different modes start lasing first. Here, the strongly confined modes located in a defect or gap compete against the spatially extended modes located above the metal stripes, which can form phase-locked supermodes.

As the third and final step, we integrate the emission power according to Equation (9) over a wavelength window $\lambda \in [630, 650 \text{ nm}]$ to obtain the emitted energy E_{out} . Following these three steps for the four different excitation modes, varying the excitation pulse energies for the setups with different numbers of DBR layers leads to the lasing thresholds shown in Figure 8.

As the MC quality factors grow with increasing number of DBR layers, also does computational run time. The introduction of additional DBR layers leads to an increment in the computational domain with the finest spatial resolution enhancing the

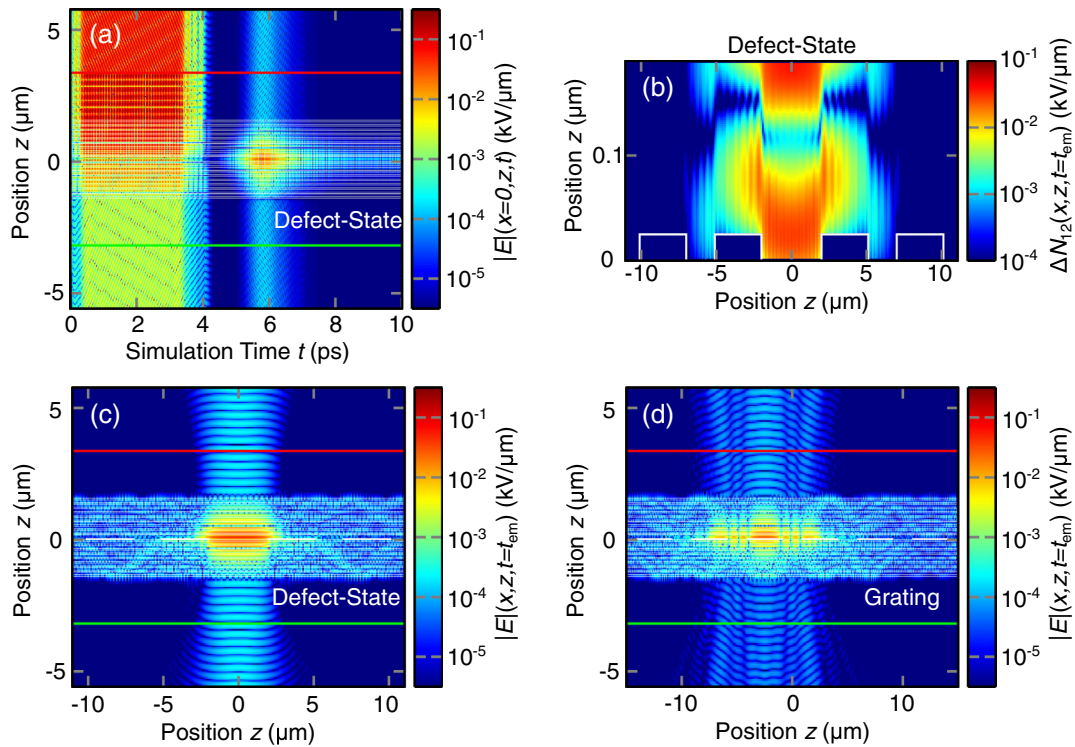


Figure 6. Electric field distributions for the 17-layer DBR defect setup, just above lasing threshold excitation. a) Cut through the center of the defect, showing the incoming excitation field $t < 4$ ps from the Tf/Sf contour (red line) and the lasing of the DBR cavity at $t \approx t_{em} = 6$ ps. b) Population inversion density ΔN_{12} of the emission transition of the four-level system, shown within the cavity at time $t_{em} = 6$ ps. c,d) Field patterns of the c) radiating defect and d) OSE mode at $t_{em} = 6$ ps as well as the scattered field within the DBR MC.

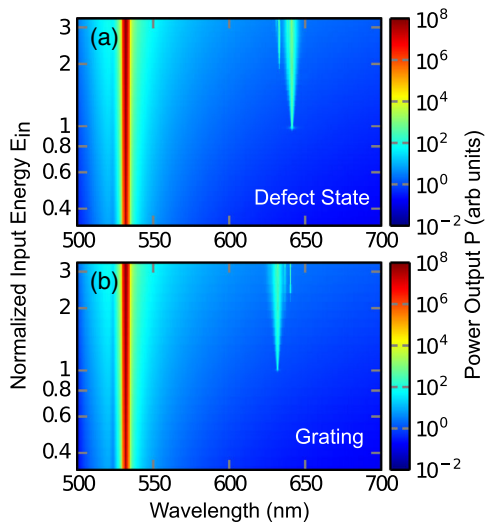


Figure 7. Wavelength-resolved scattering power $P = \int_{A_c} d\vec{f} \cdot \langle \vec{S} \rangle_T$ depending on the pump pulse input energy, showing both the reflection and transmission, as well as the emission signals for the a) defect and b) OSE for a setup including 17/2 layer pair DBRs.

computational effort significantly. Here, the simulation time for a 17/2 pair device is on the order of 2 weeks, whereas a simulation of the full 21/2 DBR stack is expected to take >2 months. We

therefore present setups with 5/2, 9/2, and 17/2 pairs of SiO₂ and TiO₂ layers to demonstrate the general trend of the lasing threshold development. To obtain comparable results, we normalize the input energies of the lasing thresholds to that of the corresponding metal stripe excitation. In all three setups, we observe the lasing threshold for on-stripe excitation (OSE) of grating to systematically move to that of the bare MC with increasing number of DBR layers. Simultaneously, for all setups, the defect lasing threshold always lies below the threshold of the bare cavity, supporting the experimental observations. Furthermore, the threshold for excitations upon a gap of the defect-free grating always lies in between the OSE and defect excitation. This can be attributed to the interplay of the two different lasing modes excited. These modes are nearly degenerate in frequency, yet do not share a strong positional overlap. One mode is formed within the gap/defect, whereas the other is located between the top DBR and a single metal stripe acting as the bottom mirror.

Evidence to this is given by the second-threshold onsets in the defect setup at $\lambda \approx 632$ nm, as shown in Figure 7a, and also the corresponding lasing threshold upon OSE, as shown in Figure 7b. Small deviations, like the thickness of the silver-layer $d_{Ag} = 25$ nm in the computational setup, lead to a stronger spectral separation of the two different modes compared with the experiment. The OSE mode in the experiment is blue-shifted (effectively a smaller cavity size) only a few nanometers in the experiment (cf. Figure 4e vs. f).

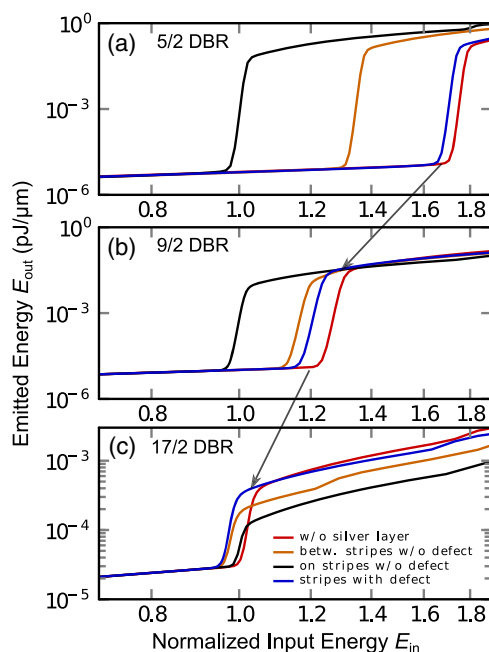


Figure 8. Lasing thresholds computed for different numbers of DBR layers, i.e., a) five, b) nine, and c) seventeen. The thresholds are normalized to the input energy of the OSE thresholds, as the onset of the thresholds shifts with the changing number of DBR layers, which directly influences both external reflection and the quality factor of the cavity. Gray arrows show the development of lasing thresholds for the pure organic and the defect-state lasing for increasing quality of the cavity. It is important to note that the defect state always shows a lower threshold than the bare organic cavity.

For the few-layer (5/2 pairs) DBRs, the metallic mirror provides the highest-quality resonance leading to the lowest lasing threshold for that system (see Figure 8a). Yet, an increase in the number of DBR layers leads to an overall shift to lower lasing threshold energies, as the cavity quality factor is enhanced. This enhancement of the DBR's quality factor in addition to the confinement of fields in the defect yields a mode with even a higher-quality factor. In turn, the defect mode provides the lowest overall lasing threshold (see Figure 8c), for a sufficiently high number of DBR layers, as demonstrated by the clear trend in the DGTD simulations for increasing the quality of the cavity. In the experimental realization including DBRs with 21/2 layer pairs, this effect is even more pronounced (cf. Figure 5). Importantly, field confinement in the defect also leads to lasing thresholds systematically lower than those of the cavity without any metal grating.

5. Conclusion

In conclusion, we investigated an organic MC with a silver grating and observed discrete states below and extended states above the potential barrier of the metal. We further showed the formation of a nondispersive DS with a high degree of localization in real space if a defect is implemented into the periodic pattern. An increase in pump intensity above lasing threshold for the

defect-free pattern leads to the formation of several equidistant lasing modes at π or 2π states of the Brillouin zone, depending on parity. In comparison, the far-field image of the pattern with defect shows lasing only for the lowest DS which is very broad in k -space indicating a very narrow and defined mode in real space as confirmed in the DGTD computations. In addition, these DGTD computations provide an in-depth insight into the lasing dynamics and enable a thorough study of the lasing thresholds for different geometries, especially a systematic scan in the number of DBR layers. Further, both the computations and experimental measurements show that the lasing threshold of the MC with a silver pattern and defect is lower compared with a bare MC without metal grating, despite additional absorption. These findings demonstrate how the incorporation of metallic films into organic MC enables fine-tuning of their lasing properties. By varying the grating or introducing defects, the lasing mode can be changed from an extended supermode with strong directionality to a strongly confined, low-threshold lasing mode with a broad angular emission.

Supporting Information

Supporting Information is available from the Wiley Online Library or from the author.

Acknowledgements

The authors gratefully acknowledge support by the Deutsche Forschungsgemeinschaft (DFG, German Research Foundation) with the DFG projects Tailored Disorder SPP 1839, no. LE 747/47-1, no. LE 747/55-1, and BU 1107/10-1, as well as the Cluster of Excellence Center for Advancing Electronics Dresden. This work was further supported by the DFG through the Würzburg-Dresden Cluster of Excellence ct.qmat (EXC 2147, project id 390858490). A.M. acknowledges funding through an individual fellowship of DFG (404587082). T.K. and K.B. acknowledge support from the DFG—Project-ID 182087777—SFB 951.

Conflict of Interest

The authors declare no conflict of interest.

Keywords

defect-state lasing, microcavities, organic lasers, photonic confinements, Tamm plasmon polaritons

Received: October 28, 2020

Revised: December 9, 2020

Published online:

- [1] E. Yablonovitch, *JOSA B* **1993**, *10*, 283.
- [2] B. I. Shklovskii, A. L. Efros, in *Electronic Properties of Doped Semiconductors*, Vol. 45, Springer Science and Business Media, New York **2013**.
- [3] K. Walzer, B. Maennig, M. Pfeiffer, K. Leo, *Chem. Rev.* **2007**, *107*, 1233.
- [4] J. Huang, M. Pfeiffer, A. Werner, J. Blochwitz, K. Leo, S. Liu, *Appl. Phys. Lett.* **2002**, *80*, 139.

- [5] K. J. Vahala, *Nature* **2003**, 424, 839.
- [6] A. Kavokin, J. J. Baumberg, G. Malpuech, F. P. Laussy, *Microcavities*, Oxford University Press, Oxford, UK **2017**.
- [7] T. Gutbrod, M. Bayer, A. Forchel, P. A. Knipp, T. L. Reinecke, A. Tartakovskii, V. D. Kulakovskii, N. A. Gippius, S. G. Tikhodeev, *Phys. Rev. B* **1999**, 59, 2223.
- [8] A. I. Tartakovskii, V. D. Kulakovskii, A. Forchel, J. P. Reithmaier, *Phys. Rev. B* **1998**, 57, R6807.
- [9] A. Mischok, R. Brückner, M. Sudzius, C. Reinhardt, V. G. Lyssenko, H. Fröb, K. Leo, *Appl. Phys. Lett.* **2014**, 105, 051108.
- [10] C. P. Dietrich, M. Karl, J. Ohmer, U. Fischer, M. C. Gather, S. Höfling, *Adv. Mater.* **2017**, 29, 1605236.
- [11] M. Bayer, T. Gutbrod, A. Forchel, T. L. Reinecke, P. A. Knipp, R. Werner, J. P. Reithmaier, *Phys. Rev. Lett.* **1999**, 83, 5374.
- [12] K. Winkler, J. Fischer, A. Schade, M. Amthor, R. Dall, J. Geßler, M. Emmerling, E. A. Ostrovskaya, M. Kamp, C. Schneider, S. Höfling, *New J. Phys.* **2015**, 17, 023001.
- [13] R. Brückner, A. A. Zakhidov, R. Scholz, M. Sudzius, S. Hintschich, H. Fröb, V. Lyssenko, K. Leo, *Nat. Photonics* **2012**, 6, 322.
- [14] F. J. Löchner, A. Mischok, R. Brückner, V. G. Lyssenko, A. A. Zakhidov, H. Fröb, K. Leo, *Superlattice Microstruct.* **2015**, 85, 646.
- [15] C. Schneider, K. Winkler, M. Fraser, M. Kamp, Y. Yamamoto, E. Ostrovskaya, S. Höfling, *Rep. Progr. Phys.* **2016**, 80, 016503.
- [16] M. Röhner, J. P. Reithmaier, A. Forchel, F. Schäfer, H. Zull, *Appl. Phys. Lett.* **1997**, 71, 488.
- [17] M. Kaliteevski, I. Iorsh, S. Brand, R. A. Abram, J. M. Chamberlain, A. V. Kavokin, I. A. Shelykh, *Phys. Rev. B* **2007**, 76, 165415.
- [18] R. Brückner, M. Sudzius, S. I. Hintschich, H. Fröb, V. G. Lyssenko, K. Leo, *Phys. Rev. B* **2011**, 83, 033405.
- [19] S. Meister, R. Brückner, M. Sudzius, H. Fröb, K. Leo, *Appl. Phys. Lett.* **2018**, 112, 113301.
- [20] S. Meister, R. Brückner, M. Sudzius, H. Fröb, K. Leo, *J. Mater. Res.* **2019**, 34, 571.
- [21] B. Liu, R. Wu, V. M. Menon, *J. Phys. Chem. C* **2019**, 123, 26509.
- [22] A. Mischok, V. G. Lyssenko, R. Brückner, F. Löchner, R. Scholz, A. A. Zakhidov, H. Fröb, K. Leo, *Adv. Opt. Mater.* **2014**, 2, 746.
- [23] P. St-Jean, V. Goblot, E. Galopin, A. Lematre, T. Ozawa, L. Le Gratiet, I. Sagnes, J. Bloch, A. Amo, *Nat. Photonics* **2017**, 11, 651.
- [24] L. Ferrier, H. S. Nguyen, C. Jamois, L. Berguiga, C. Symonds, J. Bellessa, T. Benyattou, *APL Photonics* **2019**, 4, 106101.
- [25] K. Busch, M. König, J. Niegemann, *Laser Photonics Rev.* **2011**, 5, 773.
- [26] T. Pfadler, T. Kiel, M. Stärk, J. F. M. Werra, C. Matyssek, D. Sommer, J. Boneberg, K. Busch, J. Weickert, L. Schmidt-Mende, *Phys. Rev. B* **2016**, 93, 205305.
- [27] P. B. Johnson, R. W. Christy, *Phys. Rev. B* **1972**, 6, 4370.
- [28] S.-H. Chang, A. Taflove, *Opt. Express* **2004**, 12, 3827.
- [29] A. Taflove, S. C. Hagness, *Computation Electrodynamics – The Finite-Difference Time-Domain Method*, 3rd ed., Artech House, London, **2005**.
- [30] İlker R. Çapoğlu, A. Taflove, V. Backman, *Opt. Express* **2013**, 21, 87.
- [31] A. Mischok, M. Kliem, R. Brückner, S. Meister, H. Fröb, M. C. Gather, K. Leo, *Laser Photonics Rev.* **2018**, 12, 1800054.
- [32] P. R. Rice, H. Carmichael, *Phys. Rev. A* **1994**, 50, 4318.
- [33] H. Yokoyama, S. Brorson, *J. Appl. Phys.* **1989**, 66, 4801.